Canadian Science Publishing | Transactions of the Canadian Society for Mechanical Engineering

Vibration Noise Suppression Approach Based on Random Switching Frequency (RSF) Control for Permanent Magnet Motor

Journal:	*Transactions of the Canadian Society for Mechanical Engineering*
Manuscript ID	TCSME-2020-0075.R1
Manuscript Type:	Article
Date Submitted by the Author:	04-Oct-2020
Complete List of Authors:	Li, Yong; The State Key Laboratory of Mechanical Transmissions, Chongqing University, Chongqing 400044, P. R. China; Automotive Engineering Research Institute, Jiangsu University, Zhenjiang, 212013, P. R. China Wu, Hao; Automotive Engineering Research Institute, Jiangsu University, Zhenjiang, 212013, P. R. China Si, Qiaorui; Research Center of Fluid Machinery Engineering and Technology, Jiangsu University, Zhenjiang, 212013, P. R. China Liu, Yonggang; The State Key Laboratory of Mechanical Transmissions, Chongqing University, Chongqing 400044, P. R. China
Keywords:	In-wheel motor, Unbalanced magnetic force, Electric current harmonics, PWM, Random switching Frequency
Is the invited manuscript for consideration in a Special Issue? :	Not applicable (regular submission)

Vibration Noise Suppression Approach Based on Random Switching Frequency (RSF) Control for Permanent Magnet Motor

Yong Li[1,2], Hao Wu[2], Qiaorui Si[3] and Yonggang Liu[1]

1 The State Key Laboratory of Mechanical Transmissions, Chongqing University, Chongqing 400044, China

2 Automotive Engineering Research Institute, Jiangsu University, Zhenjiang 212013, China

3 Research Center of Fluid Machinery Engineering and Technology, Jiangsu University, Zhenjiang 212013, China

Corresponding author: Yong Li

E-mail: liyongthinkpad@outlook.com

Abstract The vibration noise of the distributed drive autonomous ground vehicle (AGV) is mainly produced by the inverter-fed brushless DC permanent magnet in-wheel motor (PMIWM). It is necessary to reduce the vibration noise level of the PMIWM driven by pulse width modulation (PWM). A suppression approach of electromagnetic vibration noise for PMIWM is investigated. Firstly, the air gap magnetic field of the inverter-fed PMIWM was analyzed. The electric current harmonics and the unbalanced magnetic force (UMF) were investigated. The natural frequency and noise of the PMIWM were presented. Then, flux-weaken approach was employed to maintain the robustness of the PMIWM when a sudden drop of DC bus voltage. The random switching frequency (RSF) PWM control method based on two state Markov chain is proposed to decrease the amplitude of the harmonics caused by the switching frequency and the multiple switching frequencies. The experimental results show that the RSFPWM can not only effectively reduce the vibration noise and the inverter losses, but also improve the robustness of the PMIWM control system under unpredictable uncertainties.

Key words In-wheel motor, Unbalanced magnetic force, Electric current harmonics, PWM, Random switching Frequency

I. Introduction

The energy crisis and environmental pollution are becoming essential factors that restrict the development of the global automotive industry (Huang et al. 2017; Li et al. 2018b). The rapidly developed electric vehicles (EV), in recent years, stand for the development of next-generation vehicles in the future. The brushless DC in-wheel motor (IWM) drive system eliminating the transmission, gearbox and differential propels the vehicle directly (Chen et al. 2018; Li et al. 2019). With the development of the communication, cybernetics, artificial intelligence and sensors, autonomous ground vehicle (AGV) is supposed to improve vehicle safety and traffic efficiency. The IWM drive AGV is an essential part of the intelligent transportation system (ITS) in smart city (Huang et al. 2018). However, the IWM drive AGV, with a compact chassis structure, has large unsprung mass due to the IWM installed inside the wheel hub. The electromagnetic vibration of the IWM will be directly delivered to the vehicle body through the wheels, resulting in vehicle comfort reduction. Moreover, the vibration will further lead to a lot of noise, which brings severe harm to hearing of the people who work long time in such an environment, especially for noise-sensitive people (Song et al. 2017; Niu et al. 2017; Wang et al. 2018). With the increasing requirement of vehicle comfort, NVH performance in the automotive industry is becoming more and more important. The noise level of the IWM is a key factor to evaluate the operating performance of IWM drive AGV (Yin et al. 2017). Therefore, to provide a quiet and comfortable environment for IWM drive AGV, the vibration and noise suppression of IWM has drawn lots of attention around the world (Li et al. 2018d; Xu et al. 2018; Tang et al. 2018; Zuo et al. 2015).

The PMIWM fed by pulse width modulated (PWM) inverter is supposed to realize speed control for AGV. The stator and rotor iron losses caused by the high-order harmonic fields is more complex in the PWM inverter-fed PMIWM. What is more, the harmonic current brought by PWM inverter also leads to electromagnetic vibration noise, especially nearby the switching frequency and its multiples in the frequency range. The electromagnetic vibration brought by PWM inverter mainly contributes to the IWM noise. The radial magnetic force changing with the time and space is produced by the air-gap magnetic field of the motor. The radial magnetic force leads to periodic deformation of the stator and the seat of the motor, which brings the vibration and noise to the IWM (Jiang et al. 2017; Sun et al. 2016). The distributed drive AGV with complex drive cycle, unexpected load and wide speed range is propelled by the in-wheel motor. A large amount of time harmonics current is produced by the inverter, which leads to great harmonics magnetic field inside the air gap. The amplitude and order will be affected by the harmonics magnetic field. Sympathetic vibration may occur when the frequency of radial force wave equals with the modal frequency of the vehicle body. The vibration and noise of

the IWM, even the whole vehicle, will increase obviously (Li et al. 2018a). Therefore, the radial force is the major reason for the vibration and noise of distributed drive AGV.

To reduce or suppress the vibration and noise of the permanent magnet motor, a lot of researchers worked on the motor structure design and control strategies. Slot pole configuration can increase the vibration frequency of the cogging torque and effectively reduce the vibration amplitude of the cogging torque. In Ref Enrico et al. (2018), the slot/pole combination on the optimal motor dimensions, torque density, and the motor cost is discussed. Cogging torque, torque ripple, electromechanical performance, and the stator deformation of the machines are evaluated. The subharmonics and some of the higher order harmonics of a nine-phase 18-slot 14-pole IPM machine are canceled out (Chen et al. 2016). Deng provides a detailed finding of the influence of pole and slot combinations on vibration and noise in external rotor axial flux in-wheel motors (AFWMs) (Deng et al. 2017). Direct torque control (DTC) is verified to be effective in reducing the influence of cogging torque and vibration (Zhu et al. 2006). Gan investigates the effects of the short permanent magnet and stator flux bridge on the cogging torque reduction of three-phase 12/10-pole flux switch permanent magnet machines (Gan et al. 2017). In Ref Abdollahi et al. (2013), the cogging torque of the motor is analyzed and reduced by imposing notches into the segments. Moreover, the torque ripple and radial electromagnetic force are used to reduce motor vibration and noise. A torque ripple reduction method for a five-phase interior permanent magnet (PM) motor by shifting asymmetrical rotor poles is studied (Chen et al. 2018). A novel pattern of the connecting wire is proposed in Ref Sung et al (2012) to eliminate the pole harmonics of the torque ripple and UMF induced by the connecting wire. Zhu investigates an outer rotor flux-switching permanent-magnet (FSPM) motor and reduces the torque ripple of the motor (Zhu et al. 2017). Han proposes a two-segment motor system powered by two inverters with phase-shift pulse width modulation (PWM) to fulfill the purpose of low-torque ripple and vibration noise (Han et al. 2019). A torque sharing function (TSF) is proposed to reduce torque and voltage ripple (Ze et al. 2018). Liu proposes a new method to improve the motor torque and reduce the high-frequency harmonics of the motor (Liu et al. 2018; Liu et al. 2017). Both simulation and experimental results verify the effectiveness of the proposed control system and the copper losses minimization TSF in reducing torque and voltage ripple. An analytical model has been developed by Zhu for analyzing the radial vibration force in fractional-slot permanent-magnet machines (Zhu et al. 2010). The study can instruct the designer to lower the modular machine's vibration under different fault conditions. Valente takes advantage of the spatial distribution of the winding sets within the stator structure in a permanent-magnet machine toward achieving a controllable radial force (Valente et al. 2018). An alternative force control technique for PMSM machines is presented to obtain the suppression of selected vibration frequencies for different rotational speeds. The above-mentioned

approaches suppress the vibration and noise of the motor from some degree. Pulse width modulation (PWM) is widely employed in variable frequency speed adjust system, especially in the PWM-based inverter system. The carrier phase-shift space vector pulse width modulation (SVPWM) is applied to a 24-slot 20-pole PMSM (Miyama et al. 2018). Zhao proposed a new fault-tolerant direct thrust force control (DTFC) for a dual inverter fed open-end winding linear vernier permanent-magnet (LVPM) motor (Zhao et al. 2018) An asymmetrical space vector pulse-width modulation (SVPWM) fault-tolerant control is proposed for the five-phase permanent-magnet motor under the open-circuit condition of a single phase (Chen et al. 2017). A pseudo-random phase-switching fixed-frequency (PRPSFF) signal injection method is proposed by Wang to offset discrete harmonic spectrum and achieve sensorless control on a 2.2-kW IPMSM (Wang et al. 2018). The current-mode hysteretic buck converter is investigated to eliminate spurs from the switching noise spectrum irrespective of variations in the noise-sensitive systems (Nashed et al. 2018). The fixed switching frequency offers remarkable simplicity of the converter and filter design (Pichan et al. 2017). The fixed switching frequency algorithm is employed to ensure switching spectrum concentrated around the desired switching frequency (Guzman et al. 2016). A 2-D random-switching pulse width modulation (PWM) technique is proposed to reduce the dominant harmonic clusters and the output voltage ripple (Lai et al. 2013). Paramasivan presents an assorted carrier-variable frequency random pulse width modulation (AC-VF-RPWM) method is proposed for an inverter-fed induction motor drive to reduce the acoustic noise (Paramasivan et al. 2017). However, most of the current researches are based on the structure design, torque ripple, radial force, fixed PWM and random PWM method, which cannot effectively reduce the vibration and noise of the motor. Especially, the fixed switching frequency leads to harmonic currents in narrow bands around integral multiples of the switching frequency resulting in acoustic noise components, which are irritating to the human ear.

This paper contributes a novel approach for the suppression of electromagnetic vibration noise based on the random switch frequency (RSF) PWM control. The electric current harmonics suppression of a PWM-fed inverter for PMIWM is experimentally verified, which not only brings less iron losses than fixed PWM control and random pulse position (RPP) PWM control, but also provides the robustness of the inverter-fed PMIWM under unpredicted conditions while the AGV is operating.

The paper is organized as follows. First, the harmonics magnetic field and radial force of inverter-fed PMIWM is analyzed in Section 2. After that, in Section 3, the RSFPWM is studied to suppress the vibration noise of PMIWM. In Section 4, the iron losses of PMIWM fed by RSFPWM inverter are analyzed. The vibration noise, robustness and losses of the proposed RSFPWM are experimentally verified in Section 5. Section 6 is devoted to conclusions and future work.

II. Analysis of the harmonics magnetic field and radial UMF of inverter-fed PMIWM

A. Harmonics magnetic field analysis

The fundamental wave magnetomotive force of the stator and the harmonic magnetomotive force of the permanent magnet do not change no matter the PMIWM is fed by inverter or sine wave. But, the harmonics magnetomotive force of the stator under inverter-fed PMIWM is different from that under sinewave-fed PMIWM. There are a large number of high-order time harmonics inside the stator current of the PMIWM. The stator harmonic unbalanced magnetic field (UMF) consists of two parts. One is the harmonic EMF generated by the fundamental wave current of the stator winding. The other is harmonic EMF produced by the *h*-th order harmonic current (Zhu et al. 2018; Ma et al. 2015; Kang et al. 2018).

The total EMF of PWM-fed PMIWM can be described as

$$\begin{aligned} f(\theta,t) &= f_1\cos(p\theta-\omega_0 t-\varphi_1)+\sum f_2\cos(\nu\theta-\omega_0 t-\varphi_2) \\ &+\sum f_3\cos(\mu\theta-\mu\omega_0 t/p-\varphi_3)+\sum f_4\cos(\nu\theta-h\omega_0 t-\varphi_4) \end{aligned} \tag{1}$$

Where, $F_1\cos(p\theta-\omega_0 t-\varphi_1)$ is the fundamental wave EMF. $\sum f_2\cos(\nu\theta-\omega_0 t-\varphi_2)$ is the harmonic EMF of the stator. $\sum f_3\cos(\mu\theta-\mu\omega_0 t/p-\varphi_3)$ is the harmonic EMF of the magnet. $\sum f_4\cos(\nu\theta-h\omega_0 t-\varphi_4)$ is the harmonic EMF produced by the inverter, which leads to the vibration and noise of the PWM-fed PMIWM.

Ignoring the saturation of the iron core, the air gap magnetic field can be expressed as

$$b(\theta,t)=f(\theta,t)\lambda(\theta,t) \tag{2}$$

where, $\lambda(\theta,t)$ is the air gap magnetic conductivity.

The air gap magnetic density of inverter-fed PMIWM is described as

$$\begin{aligned} b(\theta,t) &= f_1\Lambda_0\cos(p\theta-\omega_0 t-\varphi_1)+f_2\Lambda_0\cos(\nu\theta-\omega_0 t-\varphi_2) \\ &+f_3\Lambda_0\cos(\mu\theta-\mu\omega_0 t/p-\varphi_3)+f_4\Lambda_0\cos(\nu\theta-h\omega_0 t-\varphi_4) \\ &+\sum\frac{f_1\Lambda_n}{2}\cos\left[(\pm l_1 Z_1+p)\theta-\omega_0 t-\varphi_5\right] \\ &+\sum\sum\frac{f_\mu\Lambda_n}{2}\cos\left[(\pm l_1 Z_1+\mu)\theta-\mu\omega_0 t-\varphi_6\right] \end{aligned} \tag{3}$$

The component $\sum f_4\Lambda_0\cos(\nu\theta-h\omega_0 t-\varphi_4)$ just exists in the inverter-fed PMIWM. It is produced by the *h*-th order time harmonic current of the stator winding, which generating the rotating fundamental wave magnetic field and harmonic magnetic field. That is the main reason for the vibration and noise of the inverter-fed PMWIM.

B. Radial UMF analysis

The radial harmonic electromagnetic force is caused by the high-frequency harmonic current inside the inverter. The component of radial electromagnetic force with large amplitude is generated by the interaction of the high frequency electric current harmonic magnetic field, the magnet field and the armature current. The frequency of the radial electromagnetic force mainly distributes near the switching frequency and its multiple frequencies, which are the main factors leading to high-frequency vibration and noise. The high frequency harmonic magnetic field and harmonic current are caused by the high frequency harmonic voltage from the inverter. The back EMF also affects the shape and amplitude of the harmonic magnetic field (Li et al. 2018a; Diao et al. 2017; Samad et al. 2017).

The Maxwell tensor is used to analyze the EMF of the PMIWM. The radial EMF of the stator core of the PMIWM can be expressed as

$$p_{EMF}(\theta,t)=\frac{1}{2\mu_0}\left[b^2(\theta,t)-b_t^2(\theta,t)\right] \tag{4}$$

Where, μ_0 is the air permeability. $b(\theta,t)$ is the radial air gap magnetic density of the stator core. $b_t(\theta,t)$ is the tangential air gap magnetic density of the stator core. r is the order number of the radial EMF.

As the air permeability is far smaller than the core permeability, the radial components of the flux density are far larger than the tangential components of the flux density. Eq. (4) can be simplified as

$$p_{EMF}(\theta,t)=\frac{b^2(\theta,t)}{2\mu_0} \tag{5}$$

Combining Eq. (3) and Eq. (5), the radial EMF of the PWM-fed PMIWM can be expressed as

$$p_{EMF}=\frac{1}{2\mu_0}\left\{\begin{bmatrix}\sum f_3\cos(\omega_{\mu,n}t-\mu p\theta)+\sum f_2\cos(\omega_n t-\nu p\theta+\phi)\\ +\sum f_2\cos(\omega_n t+\nu p\theta+\phi)\times\left[\Lambda_0+\sum_{i=1,2,3}^{\infty}\Lambda_i\cos(iZ\theta)\right]\end{bmatrix}\right\} \tag{6}$$

C. Harmonics current noise frequency analysis

According to the mechanical impedance theory, the vibration displacement of the motor stator is expressed as

$$L_s=\frac{2\pi R_i l_1 A_r}{(k_1+k_2)-\omega_r^2(m_1+m_2)} \tag{7}$$

Where, R_i is the inner diameter of the PMIWM. l_l is the length of the PMWIM. A_r is the amplitude of the r-order excitation wave on the stator armature. k_1 and k_2 are the equivalent stiffness of the stator core and the motor casing, respectively. m_1 and m_2 are the equivalent mass of the stator core and the motor casing, respectively.

For the PMIWM, there is no corresponding tangential displacement between the stator core and the motor casing (Luo et al. 2012; Song et al. 2018). The noise frequency of the PMIWM is mainly determined by the order of the EMF. The natural frequency of the stator is expressed as

$$f_s = \frac{1}{2\pi}\sqrt{\frac{k_1 + k_2}{m_1 + m_2}} \tag{8}$$

The sound power level (SPL) radiated by the *r*-order vibration mode of the PMIWM stator can be calculated from the following equation:

$$L = 10\lg\left[\frac{1}{n}\sum_{i=1}^{n}10^{0.1(l_{pi}-v_i)}\right] - v_2 - v_3 + 10\lg\frac{s}{s_0} \tag{9}$$

Where, l_{pi} is the sound pressure level of the spot *i*. v_i is the correction value of the background noise at the spot *i*. n is the spot number. v_2 is the environmental reflection correction value. v_3 is the correction value of the temperature and environment. s is the measuring surface area. s_0 is the reference area.

III. RSFPWM control approach

A. Inverter-fed PMIWM

The drive scheme of inverter-fed PMIWM is shown in Fig. 1. S_a, S_b and S_c are the three phase drive signal of the inverter, respectively, which can be expressed in the following.

$$\begin{cases} S_a = \begin{cases} 1 & s_1 > 0, s_4 \le 0 \\ 0 & s_1 > 0, s_4 \ge 0 \end{cases} \\ S_b = \begin{cases} 1 & s_3 > 0, s_6 \le 0 \\ 0 & s_3 > 0, s_6 \ge 0 \end{cases} \\ S_c = \begin{cases} 1 & s_5 > 0, s_2 \le 0 \\ 0 & s_5 > 0, s_2 \ge 0 \end{cases} \end{cases} \tag{10}$$

The voltage of the PMIWM is expressed as

$$\begin{cases} u_a = u_m \sin \omega t \\ u_b = u_m \sin\left(\omega t - 2\pi/3\right) \\ u_c = u_m \sin\left(\omega t + 2\pi/3\right) \end{cases} \tag{11}$$

Where, u_m is the voltage amplitude. ω is the electrical angle of rotor position.

The SVPWM modulation technology has been widely used in motor control. The three-phase inverter is shown in Fig. 3, in which 6 IGBTs are employed as the 6 switches. Supposing 1 represents the turning on the state of the switch and 0

represents the turning off state of the switch. The voltage vectors 100, 110, 010, 011, 001, 101, 000 and 111 constituting 8 working modes. Each vector has the same amplitude. The phase angle between the vector and its adjacent vector is 60 degree. The amplitudes of the vector 000 and 111 are 0 (Bauw et al. 2018; Wen et al. 2018; Hara et al. 2018). The size and position of the basic voltage space vector is shown in Fig. 2.

B. DC bus voltage control

A flux-weaken approach based on current compensation of negative *q*-axis is used to avoid the sudden decrease of DC bus voltage of PMIWM in this paper. The *d*-axis current of the PMIWM can be adjusted to operate at a constant speed by judging the voltage vector and real-time DC bus voltage when the DC bus voltage is lower than the target speed, and the voltage limit ellipse intersects with the current limit ellipse. The current trajectory when DC bus change is shown in Fig. 3. u_{dc1}, u_{dc2}, u_{dc3} and u_{dc4} are DC bus voltage, respectively. The voltage limited ellipse will reduce under constant speed when the DC bus voltage decreases. The DC bus voltage will drop from u_{dc1} to u_{dc2} while the turning point of PMIWM changes from *A* to *C* and *K*. Flux weaken control is used to keep the PMIWM operating at a constant speed.

The MTPA method is employed under the base speed to increase the output torque under the limitation of current capacity of the inverter. This method can minimum the stator current of the PMIWM under the same electromagnetic torque, which is beneficial to reduce the copper loss and improve the utilization of stator current. The Lagrange's extremum theorem is used to calculate the *d*-axis current and the *q*-axis current to obtain the maximum torque by using the minimum current.

$$\begin{cases} i_d = \dfrac{\varphi_f - \sqrt{\varphi_f^2 + 8\left(L_q - L_d\right)^2 i_s^{\,2}}}{4\left(L_q - L_d\right)} \\ i_d = \sqrt{i_s^{\,2} - i_d^{\,2}} \end{cases} \tag{12}$$

The negative direct axis current compensation approach is used above the base speed, by which the output voltage command from current regulator and the DC bus voltage amplitude of the PMIWM can be detected continuously. The amplitude of the *d*-axis current is increased to make the working point of the PMIWM move left and return to the voltage ellipse once the output voltage vector of the current regulator exceeds the voltage limit value. The error between the output voltage vector and limited voltage of the inverter is regulated as the compensation of i_d under MTPA control, with which the motor can obtain better performance without complex computation in the flux weaken area.

The basic speed can be expressed as

$$\omega = \frac{u_{\lim}}{p\sqrt{\left(L_q i_{\lim}\right)2 + \psi_f{}^2 + \frac{(L_d + L_q)G^2 + 8\psi_f L_d G}{16(L_d - L_q)}}} \tag{13}$$

Where, $G = -\psi_f + \sqrt{\psi_f{}^2 + 8(L_d - L_q)^2 i_{\lim}{}^2}$

It can be seen from Eq. 13 that the turning speed is proportional to the DC bus voltage.

B. RSFPWM control

The output voltage of the inverter is just controlled by the duty ratio of the IGBT. The spectrum distribution of the output voltage can be changed by the switching frequency and the on location of the pulse. The discrete spectrum of the output voltage and the current of the inverter will be converted into a wide and uniform continuous spectrum by randomly changing either of the switching frequencies or the switching position. The harmonic components with large amplitudes near the carrier frequency and its multiple can be effectively suppressed, by which the vibration noise and electromagnetic interference can be effectively reduced.

The random modulation technology is a flexible method to suppress harmonic at switching frequency. The random regulation of each modulation technique can be adjusted flexibly by randomly changing the switching period or pulse position. The random probability of each modulation scheme can also be flexibly configured and changed (Kumar et al. 2016; Brudny et al. 2015). The RSFPWM control diagram is shown in Fig. 4.

The carrier frequency of the RSFPWM inverter is described as

$$f_s = f_{s0} + r_i \Delta f \tag{14}$$

Where, f_s is the switching frequency. f_{s0} is the central frequency. $\triangle f$ is the maximum threshold of the switching frequency with the random number r_i, $-1 \le r_i \le 1$.

The harmonics spectrum changes in a corresponding range with the switching frequency. However, the switching frequency has an upper limited value due to the high switching loss and a lower limited value due to the system stability. The switching frequency is a random sequence with upper frequency and lower limit frequency. The frequency of high order electric current harmonics of the inverter changes with the random number. Therefore, the spectrum distribution of high order electric current harmonics is depended by the random number (Xia et al. 2013).

The diagram of the random switching function is shown in Fig. 5. The drive signal of the RSFPWM can be expressed as

$$u\left(t-t_k\right)=\begin{cases}1, & \varepsilon_k T_k \le t-t_k \le \left(\varepsilon_k+d_k\right)T_k \\ 0, & t-t_k<\varepsilon_k T, t-t_k>\left(\varepsilon_k+d_k\right)T_k\end{cases} \tag{15}$$

Where, t_k , ε_k and d_k are state variables, $0 \le d_k+\varepsilon_k \le 1$.

The randomness of RSFPWM control can be defined as

$$R_T=\frac{T_2-T_1}{T_s} \tag{16}$$

Where, T_2 is the maximum switching period. T_1 is the minimum switching period. T_s is the average switching period.

$$\begin{cases} f_{\min} \ge \Delta f+5f_1 \\ f_{\max} \le \dfrac{\left(f_{h\max}-13\right)}{4}\end{cases} \tag{17}$$

Where, Δf_δ is bandwidth constant. f_{hmax} is the maximum allowable harmonic frequency of the inverter.

C. Random number generation and random performance evaluation

The random number is indispensable for the implementation of RSFPWM. The ideal random number sequence should distribute uniformly in the whole frequency band. The harmonic dispersion performance cannot be obtained if the period of the random sequence is small and the probability density is shifted to the left or right in the whole period (Zhu et al. 2015; Xia et al, 2014). The mixed congruence method is used to obtain the random number based on the principle of congruence operation in number theory. The random number distribution by mixed congruence method is shown in Fig. 6.

$$\begin{cases} x_{n+1}=Mod\left(\lambda x_n+D,K\right) \quad (C>0) \\ Z_{n+1}=\dfrac{x_{n+1}}{K}\end{cases} \tag{18}$$

Where n is 0, 1, 2, 3, …., x_0 is the random number seed, which is any positive real number. Mod is remainder operator. λ is positive integer. D is nonnegative positive integer. K is the modulus, the value of which is larger than x_0, λ and D.

Random number distribution test is employed to evaluate the random performance. Suppose the range (0, 1) is divided into k equal parts. $\left(\frac{i-1}{k},\frac{i}{k}\right)$ is the i-th range. The statistic η can be expressed as

$$\eta = \sum_{i=1}^{k} \frac{\left(n_i - \frac{N}{k}\right)^2}{\frac{N}{k}} \tag{19}$$

The statistic η gradually obedience to χ^2 distribution of (k-1). Suppose the testing is described as

$$H_o : F(x) = F_o(x); H_1 : F(x) \neq F_o(x) \tag{20}$$

Where, $F_o(x)$ is the uniform distribution in the range (0, 1), which can be expressed as $F_o(x) = \begin{cases} 0 & x < 0 \\ x & 0 \le x < 1 \\ 1 & x \ge 1 \end{cases}$. H_o will be identified when the significance level a=0.05.

IV. RSFPWM suppression method based on Markov chain

The generation of random numbers should completely satisfy the uniform distribution in theory. However, in practical application, the mathematical expectation of random numbers is greater or smaller than the theoretical expectation. In that case, lots of harmonic components will be generated around the multiple of switching frequency, which does not suppress the vibration noise, may lead to worse condition.

A. Markov process theory

To effectively solve the above-mentioned problem, the RSP-PWM based on Markov chain is proposed in this section. The Markov process has been continuously improved and developed in computer science, physics, biology, automatic control and other fields by a lot of scholars since it is proposed by Andrei Markov in 1906. The Markov process can be described as the past state is all contained in the current state and the future state has no relationship with the past state, which can only be obtained from the current state.

The transition probability of the discrete event can be expressed as

$$P_{ij}(m,n) = P\{X_n = j \mid X_m = i\}, (i,j) \in S \tag{21}$$

Where, P_{ij} is the transition probability. S=$\{a_1, a_2, \ldots, a_n\}$ is state space. n and m are the event occurring time, respectively. i and j are the state, respectively.

The transition probability in the Markov process can be expressed as a $n \times m$ order matrix. Each element in the matrix is non-negative, and the sum of all elements in each row is 1.

$$P = \{P_{ij}, i, j \in S\} = \begin{bmatrix} p_{11} & p_{12} & \cdots & p_{1M} \\ p_{21} & p_{22} & \cdots & p_{2M} \\ \mathrm{M} & \mathrm{M} & \mathrm{O} & \mathrm{M} \\ p_{N1} & p_{N2} & \mathrm{L} & p_{NM} \end{bmatrix} \tag{22}$$

B. RSF-PWM model based on Markov chain

From the Markov theory, it can be found that the greater the state space of Markov chain, the better results will be obtained. However, the computation will be increased with the dimensions of state space. Two state Markov chain is employed into the RSFPWM control to evenly distribute the RSF and current spectrum, which is supposed to suppress the motor vibration and noise.

The frequency algorithm in the RSFPWM is

$$f_{n+1} = f_s + s \times R \tag{23}$$

Where, f_{n+1} is the switching frequency at the time of n+1. F_s is the nominal switching frequency. s is the random number, $-1 \le s \le 1$. R is the random gain.

Assume the nominal switching frequency is f_s. It is called state 1 when the switching frequency is larger than the nominal switching frequency. In other case, it is called state 2. The Markov chain is employed to shift between state 1 and state 2, which guarantees that there is no switching frequency larger or smaller than the nominal switching frequency and reduces the current fluctuation effectively. The two state Markov chain diagram is shown in Fig. 7.

The transition probability of two state Markov chain can be expressed as

$$P = \begin{bmatrix} P_t & 1-P_t \\ 1-P_t & P_t \end{bmatrix} \tag{24}$$

Where, P_t is the transition probability.

The transition probability P_t and random gain R will bring influence to the control effect of the RSFPWM.

C. Power spectral density analysis

The power spectral density of the random signal is equal to the Fourier transform of the self-correlation function of the random signal. The spectrum can be obtained by converting the time variable into the frequency variable (Xia et al. 2015). The truncation function of $x(t)$ can be expressed as:

$$x_T(t) = \begin{cases} x(t) & |t| < T \\ 0 & |t| \ge T \end{cases} \tag{25}$$

The Fourier transform of $x(t)$ is

$$x_T(t) = \frac{1}{2\pi}\int_{-\infty}^{+\infty} F(j\omega, T)e^{j\omega t}\mathrm{d}t \tag{26}$$

The function of the power spectral density can be expressed as

$$s(\omega) = \lim_{T\to\infty}\frac{E\left[\left|F(j\omega, T)\right|\right]^2}{2T} \tag{27}$$

Where, E is the statistical expectation.

V. Loss of RSFPWM-fed inverter

The PMIWM iron losses caused by the random carrier wave ratio of the inverter are investigated in this section. The magnetic flux density of PMIWM should be firstly calculated to obtain the iron losses. The equation of magnetic field is shown as

$$-\nabla\mathrm{g}\left(\frac{1}{\mu}\nabla A\right) = J_a + \frac{1}{\mu_0}\left(\frac{\partial M_y}{\partial x} - \frac{\partial M_x}{\partial y}\right) \tag{28}$$

Where, A is the vector magnetic potential. U is the permeability. J_a is the armature current density. M is the magnetization direction length of the permanent magnet.

The iron loss caused by the RSFPWM-fed inverter can be expressed as

$$P_{Fe} = P_c + P_h = \sum K_e\left(fB_m\right)^2 g + \sum K_h f B_m^2 g \tag{29}$$

Where, P_c and P_h are eddy current and hysteresis loss respectively. K_e and K_h are eddy current and hysteresis loss coefficients respectively. f is the alternating frequency of magnetic field in stator and rotor core. B_m is the magnetic flux density amplitude. g is the mass of the core.

The iron losses can be calculated in the finite element method (FEM) analysis software with fixed carrier wave ratio, RPP carrier wave ratio and RSF carrier wave ratio, which are shown in Table. 1. It can be seen that the iron losses under random carrier wave ratio are lower than that under fixed carrier wave ratio 30, 40 and 50. The amplitude of harmonic component in the output voltage of the inverter under fixed carrier wave ratio is larger than that under random carrier wave ratio, which brings more iron losses.

VI. Vibration and noise experiments

A. Test bench setup

To objectively demonstrate the vibration noise of the four in-wheel motor drive AGV, it is necessary to improve the traditional testing method. The vibration and noise of the in-wheel motor should be measured with a certain load. And, any other noise should not be brought to the system during the testing. The noise testing platform shown in Fig. 8 for PMIWM in AGV is established. The microphone is installed near the PMIWM, while the vibration sensor is pasted on the bracket of the stator.

The parameters of the PMIWM are illustrated in Table 2. The test platform mainly consists of the PMIWM, motor controller, battery, hardware protection circuit, LMS acquisition system and a laptop. The motor controller is used to obtain the feedback of the current, voltage and speed. It also generates PWM control signals to drive the IGBT inside the controller (Li et al. 2018c). The PMIWM is operating at a constant speed 500 r/min and a sudden load 4 Nm is implanted on the motor at 0.08s. The diagram of the PMIWM control system is shown in Fig. 9.

B. Analysis of electric current harmonic suppression

The current clamp is used to obtain the current signal of inverter-fed PMIWM under traditional fixed PWM control and the proposed RSFPWM control. The frequency response of phase-a current under fixed PWM control with 50 r/min and a constant load of 5 Nm are shown in Fig. 10. In Fig. 10(a), it can be seen that the harmonics distribute mainly at low-frequency range and the low frequency of electric current harmonics less than 3000 Hz accounts for a higher proportion than the high frequency of that. The maximum amplitude of the vibration is 25.8 A, which happens at 80 Hz. The harmonics amplitude will lead to resonance, causing severe vibration noise furtherly. The frequency response of phase-a current under RPPPWM control method with 50 r/min and a constant load of 5 Nm is shown in Fig. 10(b), we can see that the harmonics distribute mainly at low-frequency range and the low frequency of electric current harmonics less than 2000 Hz accounts for a higher proportion than the high frequency of that. From Fig. 10(b), it can be seen that the maximum amplitude of the phase-a current is appropriately 12.5 A at 80 Hz. Fig. 10(c) shows that the harmonics distribute mainly at low-frequency range and the low frequency of electric current harmonics lower than 800 Hz accounts for a higher proportion than the high frequency of that. The maximum amplitude of the vibration is 2.9 A, which happens at 80 Hz.

Compared with Fig. 10(a) and Fig. 10(b), the harmonics amplitudes in Fig. 10(c) are greatly reduced in low-frequency range and re-distributed in a wide frequency range by the RSFPWM control. It can be concluded that the electric current harmonics can be effectively suppressed by the proposed RSFPWM control approach.

To further analyze the frequency response of phase-a current with the fixed PWM control, the RPPPWM control and the proposed RSFPWM control, the frequency response of phase-a current under the above-mentioned different control approaches with 100 r/min, 200 r/min, 300 r/min, 400 r/min, 500 r/min and a constant load 5 Nm are shown in Fig. 11(a), Fig. 11(b) and Fig. 11(c), respectively. From Fig. 11(a), Fig. 11(b) and Fig. 11(c), it can be seen that the amplitude of frequency response of phase-a current with the proposed RSFPWM control is smaller than that of the fixed PWM control and RPPPWM control method under 100 r/min, 200 r/min, 300 r/min, 400 r/min and 500 r/min, respectively. It can be concluded that the electric current harmonic can be effectively suppressed by the proposed Markov chain-based RSFPWM control approach.

C. Analysis of vibration noise

To investigate the effect of electric current harmonic to the vibration and noise under100 r/min, 200 r/min, 300 r/min, 400 r/min and 500 r/min with the fixed PWM control, RSPPWM control and the proposed RSFPWM control method, the characteristics of vibration noise under a constant load 2 Nm should be analyzed. Fast Fourier transform (FFT) is employed to obtain the spectrum of vibration and noise. The frequency response of vibration and noise with the different control schemes are shown in Fig. 12, Fig. 13 and Fig. 14, respectively.

The frequency response of vibration on *x*-axis and *y*-axis with fixed PWM control are shown in Fig. 12(a) and Fig. 12(b), respectively. It can be seen the vibration spectrum mainly distributes from 0 Hz to 1000 Hz and from 3000 Hz to 4000 Hz on the *x*-axis and *y*-axis, respectively. The largest vibration amplitude at 3800 Hz is about 0.86 m/s^2 under a speed of 500 r/min on the *x*-axis. And, the largest vibration amplitude is about 0.22 m/s^2 under a speed of 300 r/min on the *y*-axis. The noise under 100 r/min, 200 r/min, 300 r/min, 400 r/min and 500 r/min with the fixed PWM control method are tested and shown in Fig. 12(c). The spectrum of the noise mainly distributes from 0 Hz to 1000 Hz. The maximum amplitude of the noise SPL at 500 r/min under 800 Hz is 0.052 $\times 100$ *dB*. It can be concluded that the noise mainly comes from the vibration caused by the electric current harmonics with the fixed PWM control. The noise amplitude also increases with the motor speed at the same frequency. From Fig. 12(a), Fig. 12(b) and Fig. 12(c), we can see the amplitude of vibration noise increase obviously with the motor speed, which indicates the speed has a great effect on the vibration noise.

The frequency response of vibration on *x*-axis and *y*-axis with the RPPPWM control are shown in Fig. 13(a) and Fig. 13(b), respectively. It can be seen that the vibration spectrum mainly distributes from 0 Hz to 1000 Hz and from 3000 Hz to 4000 Hz on the *x*-axis and *y*-axis, respectively. The largest vibration amplitude at 3800 Hz is about 0.43 m/s^2 under the speed of 400 r/min on the *y*-axis. And, the largest vibration amplitude is about 0.08 m/s^2 under the speed of 500 r/min on the *x*-axis. The vibration amplitude under100 r/min, 200 r/min, 300 r/min, 400 r/min and 500 r/min with the RPPPWM control are much smaller than that with the fixed PWM control. The noise under 100 r/min, 200 r/min, 300 r/min, 400 r/min and 500 r/min with the RPPPWM control method are tested and shown in Fig. 13(c). The spectrum of the noise also mainly distributes from 0 Hz to 1000 Hz. The maximum amplitude of the noise SPL at 500 r/min under 800 Hz is 0.048 ×100 *dB*. The noise amplitude also increases with the motor speed at the same frequency. From Fig. 13(a), Fig. 13(b) and Fig. 13(c), we can see the amplitude of vibration noise increase obviously with the motor speed, which indicates the speed has a great effect on the vibration noise with the RPPPWM control method.

The frequency response of vibration on *x*-axis and *y*-axis with the RSFPWM control are shown in Fig. 14(a) and Fig. 14(b), respectively. The largest vibration amplitude at 3800 Hz is about 0.23 m/s^2 under the speed of 400 r/min on the *x*-axis. And, the largest vibration amplitude is about 0.03 m/s^2 under the speed of 300 r/min on the *y*-axis. The vibration amplitude under100 r/min, 200 r/min, 300 r/min, 400 r/min and 500 r/min with the RSFPWM control are much smaller than that with the fixed PWM control and the RPPPWM control. The noise under 100 r/min, 200 r/min, 300 r/min, 400 r/min and 500 r/min with the proposed RSFPWM control method are also tested and shown in Fig. 14(c). The spectrum of the noise also mainly distributes from 0 Hz to 1000 Hz. The spectrum of the noise also mainly distributes from 0 Hz to 1000 Hz. The maximum amplitude of the noise SPL at 500 r/min under 800 Hz is 0.052 ×100 *dB*. The noise amplitude increases with the motor speed at the same frequency. From Fig. 14(a), Fig. 14(b) and Fig. 14(c), we can see the amplitude of vibration noise increase obviously with the motor speed, which indicates the speed has a great effect on the vibration noise with the RSFPWM control method.

Compared with the results with fixed PWM control in Fig. 12 and RPPPWM control in Fig. 13, the amplitudes of vibration noise in Fig. 14 with the proposed RSFPWM control are obviously reduced.

To clearly demonstrate the advantages of the proposed RSFPWM control approach, numerical analysis of comparison results of vibration acceleration and noise under different control are shown in Table 3 and Table 4. From the experimental results in Fig. 12, Fig. 13, Fig. 14, Table 3 and Table 4, it can be found that the RSFPWM control scheme can effectively suppress the amplitude of the vibration noise caused by the electric current harmonics in PWM-fed inverter for PMIWM. The spectrum of the electric current harmonics can also be reduced. However, the spectrum of the

vibration mainly distributes from 0 Hz to 1000 Hz, 3000 Hz to 4000 Hz on the *x*-axis, and from 0 Hz to 1000 Hz on the *y*-axis, which is not uniform with the RSFPWM control method.

D. Inverter Losses analysis

The losses caused by the fixed carrier wave ratio and random carrier wave ratio are obtained in the testing. The iron loss caused by the fixed carrier wave ratio and the random carrier wave ratio are shown in Table 5. It can be seen the iron loss caused by random carrier wave ratio is lower than that caused by fixed carrier wave ratio. The experimental results agree well with the above-mentioned simulation results, which indicate that the iron loss caused by RSFPWM approach is much lower than that caused by fixed PWM method.

From Fig. 15 we can see that the experimental results of iron losses of the PWM-fed inverter are a little bit more than that of the simulation results, due to the stray losses of the inverter happens in the experiments. It can be concluded that not only the experimental results agree well with the simulation results, but also the proposed RSFPWM control approach brings less iron loss than the fixed PWM control and RPPPWM control method.

E. Robustness and accuracy of the proposed control scheme

The flux weakening control method with negative direct axis current compensation under a case of large DC bus voltage drop is verified in this section. The curves of DC bus voltage, speed feedback and output torque are shown in Fig. 16(a), Fig. 16(b) and Fig. 16(c), respectively. It can be seen from Fig. 16 that the motor speed has a sudden fluctuation when the DC bus voltage drops from 72 V to 60 V. However, the motor maintains a constant speed 50 r/min due to the flux weakening control method with negative direct axis current compensation method. The results verified that the flux weakening control method can not only effectively maintain the PMIWM operates at the constant speed when there is a large drop on the DC bus voltage, but also has fast computation speed and robustness.

VII. Conclusions

To reduce the vibration noise of the inverter-fed PMIWM in distributed drive AGV, a novel suppression approach of electromagnetic noise is investigated in this paper. A case study of RSFPWM control based on two state Markov chain is implemented on an 8-kW PMIWM in the study. The experimental results demonstrate that: Firstly, the amplitudes of the harmonic currents with RSPPWM control under different speed are smaller than that with fixed PWM control and RPPPWM control. Secondly, compared with the fixed PWM control and RPPPWM control, the proposed RSFPWM control approach based on two state Markov chain can effectively reduce the amplitude of the vibration noise spectrum of

the PWM-fed PMIWM in distributed drive AGV. Thirdly, the proposed RSFPWM control approach brings less iron loss than the fixed PWM control and RPPPWM control method, which helps improving the inverter efficiency. Forth, the flux weakening control method is employed not only to effectively maintain the PMIWM operates at the constant speed when there is a large drop on the DC bus voltage, but also has fast computation speed and robustness.

Moreover, further investigation will be focused on the RSFPWM-fed inverter efficiency during constant power, flux-weakening region, parameters changes on the robustness, and suppression of the harmonic current in a wide range of spectrum in the future.

Acknowledgements

This project is supported by Opening Foundation of the State Key Laboratory of Mechanical Transmissions (Grant No. SKLMT-KFKT-201805), National Natural Science Foundation of China (Grant No. 51705213) and China Postdoctoral Science Foundation (Grant No. 2019M660105 and Grant No. 2020T130360).

REFERENCES

Abdollahi, S.E., and Vaez-Zadeh, S., 2013. Reducing Cogging Torque in Flux Switching Motors With Segmented Rotor. IEEE Trans. Magn. **49**(10): 5304-5309. doi: 10.1109/TMAG.2013.2260347.

Bauw, G., Balavoine, F., Cassoret, B., Ninet, O., and Romary, R. 2018. Equivalent Circuit of PWM-Fed Induction Machine With Damper Winding for Noise and Vibration Reduction. IEEE Trans. Ind. Appl. **54**(5): 4147-4155. doi: 10.1109/TIA.2018.2831635.

Brudny, J.F.., Szkudlapski, T., Morganti, F., and Lecointe, J.P. 2015. Method for Controlling the PWM Switching, Application to Magnetic Noise Reduction. IEEE Trans. Ind. Electron. **62**(1): 122-131. doi: 10.1109/TIE.2014.2327583.

Chen, Q., Liu, G., Zhao, W.X., Qu, L., and Xu, G.H. 2017. Asymmetrical SVPWM Fault-Tolerant Control of Five-Phase PM Brushless Motors. IEEE Trans. Energy Convers. **32**(1): 12-22. doi: 10.1109/TEC.2016.2611620.

Chen, Q., Xu, G., Liu, G., Zhao, W., Liu, L., and Lin, Z. 2018. Torque Ripple Reduction in Five-Phase IPM Motors by Lowering Interactional MMF. IEEE Trans. Energy Convers. **65**(11): 8520-8531. doi: 10.1109/TIE.2018.2807392.

Chen, X., Wang, J.B., Vipulkumar, I., and Panagiotis, L. 2016. A Nine-Phase 18-Slot 14-Pole Interior Permanent Magnet Machine With Low Space Harmonics for Electric Vehicle Applications. Theory and Design. Second Edition. IEEE Trans. Energy Convers. **31**(3): 860-871. doi: 10.1109/TEC.2016.2538321.

Chen, T., Xu, X., Chen, L., Jiang, H.B., Cai, Y.F. , and Li, Y. 2018. Estimation of longitudinal force, lateral vehicle speed and yaw rate for four-wheel independent driven electric vehicles. Mech. Syst.and Signal process. **101**(2):377-388. doi: 10.1016/j.ymssp.2017.08.041.

Deng, W.Z., Zuo, S.G., Lin, F., and Wu, S.L. 2017. Influence of pole and slot combinations on vibration and noise in external rotor axial flux in-wheel motors. IET Electr. Power Appl. **11**(4): 586-594. doi: 10.1049/iet-epa.2016.0788.

Diao, X.Y., and Zhu, H.Q. 2017.Survey of decoupling control strategies for bearingless synchronous reluctance motor. J. Jiangsu Univ. (Nat. Sci. Ed.). **38**(6): 687-695. doi: 10.3969/j.issn.1671-7775.2017.06.012.

Enrico, C., Nicola, B., Sunny, Z., and Matthias, K. 2018. Design and Performance Comparison of Fractional Slot Concentrated Winding Spoke Type

Synchronous Motors With Different Slot-Pole Combination. IEEE Trans. Ind. Appl. **54**(3): 2276-2284. doi: 10.1109/TIA.2018.2807382.

Gan, C., Wu, J.H., Shen, M.J., Kong, W.B., Hu, Y.H., and Cao, W.P. 2017. Investigation of Short Permanent Magnet and Stator Flux Bridge Effects on Cogging Torque Mitigation in FSPM Machines. IEEE Trans. Energy Convers. **33**(2): 845-855. doi: 10.1109/TEC.2017.2777468.

Guzman, R., Vicuña, L., Morales, J., Castilla, M., and Matas, J. 2016. Sliding-Mode Control for a Three-Phase Unity Power Factor Rectifier Operating at Fixed Switching Frequency. IEEE Trans. Power Electron. **31**(1): 758-769. doi: 10.1109/TPEL.2015.2403075.

Han, X., Jiang, D., Zou, T., Qu, R., and Yang, K. 2019. Two-Segment Three-Phase PMSM Drive With Carrier Phase-Shift PWM for Torque Ripple and Vibration Reduction. IEEE Trans. Power Electron. **34**(1): 588-599. doi: 10.1109/TPEL.2018.2824808.

Hara, T., Ajima, T., Tanabe, Y., Watanabe, M., Hoshino, K., and Oyama, K. 2018. Analysis of Vibration and Noise in Permanent Magnet Synchronous Motors With Distributed Winding for the PWM Method. IEEE Trans. Ind. Appl. **54**(6): 6042-6049. doi: 10.1109/TIA.2018.2847620.

Huang, Y.J., Fard, S.M., Khazraee, M., Wang, H., and Khajepour, A. 2017. An adaptive model predictive controller for a novel battery-powered anti-idling system of service vehicles. Energy.**127**(4): 318-327. doi: 10.1016/j.energy.2017.03.119.

Huang, Y.J., Wang, H., Khajepour, A., Li， B. and Hu, C. 2018. A review of power management strategies and component sizing methods for hybrid vehicles. Renew. sustain. energy rev. **96**:132-144. doi: 10.1016/j.rser.2018.07.020.

Jiang, H.B., Li, C.X., Ma, S.D., Ding, S.H., and Zhang, C. 2017. Path tracking control of automatic parking for intelligent vehicle based on non-smooth control strategy. J. Jiangsu Univ. (Nat. Sci. Ed.). **38**(5): 497-502. doi:10.3969/j.issn.1671-7775.2017.05.001.

Kang, H.G.., Son, Y.D., and Kim, G.T. 2018. The Noise and Vibration Analysis of BLDC Motor Due to Asymmetrical Permanent-Magnet Overhang Effects. IEEE Trans. Ind. Appl. **44**(5): 1569-1577. doi: 10.1109/TIA.2008.2002278.

Kumar, A.C., and Narayanan, G. 2016. Variable-Switching Frequency PWM Technique for Induction Motor Drive to Spread Acoustic Noise Spectrum With Reduced Current Ripple. IEEE Trans. Ind. Appl. **52**(5): 3927-3938. doi: 10.1109/PEDES.2014.7042071.

Lai, Y.S., Chang, Y.T., and Chen, B.Y. 2013. Novel Random-Switching PWM Technique With Constant Sampling Frequency and Constant Inductor Average Current for Digitally Controlled Converter. IEEE Trans. Ind. Electron. **60**(8): 3126-3135. doi: 10.1109/TIE.2012.2201436.

Liu, G.H., Xu, G.H., Zhao, W.X., Du, X.X.., and Chen, Q. 2017. Improvement of Torque Capability of Permanent-Magnet Motor by Using Hybrid Rotor Configuration. IEEE Trans. Energy Convers. **32**(3): 953-962. doi: 10.1109/TEC.2017.2665686.

Liu, G.H., Zeng, Y., Zhao, W.X., and Ji, J.H. 2018. Permanent Magnet Shape Using Analytical Feedback Function for Torque Improvement. IEEE Trans. Energy Convers. **65**(6): 4619-4630. doi: 10.1109/TIE.2017.2772142.

Li, X.H.., Sun, Y.Y., Shen, T. 2018. Vibration stability analysis of dual motor harmonic synchronous excitation nonlinear vibration conveyer. Trans. Can. Soc. Mech. Eng. **42**(4): 419-426. doi: 10.1139/tcsme-2018-0055.

Li, Y., Deng, H.F., Xu, X., and Wang, W.J. 2019. Modelling and testing of in-wheel motor drive intelligent electric vehicles based on co-simulation with Carsim/Simulink. IET Intell. Transp. Syst. **13**(1):115-123. doi: 10.1049/iet-its.2018.5047.

Li, Y., Li, B., Sun, X., and Sun, X.D. 2018a. A nonlinear decoupling approach using RBFNNI-based robust pole placement for a permanent magnet in-wheel motor. IEEE Access. **6**(1): 1844-1854. doi: 10.1109/ACCESS.2017.2780286.

Li, Y., Xu X,. and Wang, W.J. 2018b. GA-BPNN Based Hybrid Steering Control Approach for Unmanned Driving Electric Vehicle with In-Wheel Motors. Complexity. 1-15. doi: 10.1155/2018/6132139.

Li, Y., Zhang, B.H., and Xu, X. 2018c. Robust control for permanent magnet in -wheel motor in electric vehicles using adaptive fuzzy neural network with inverse system decoupling. Trans. Can. Soc. Mech. Eng. **42**(3): 286-297. doi:10.1139/tcsme-2018-0027.

Li, Y., Zhang, B.H., and Xu, X. 2018d. Decoupling control for permanent magnet in-wheel motor using internal model control based on back

propagation neural network inverse system. Bull. Pol. Acad. Sci.-Tech. Sci. **66**(6): 1-12. doi:10.24425/bpas.2018.125944.

Luo, Y., and Tan, D. 2014. Study on the Dynamics of the In-Wheel Motor System. IEEE Trans. Veh. Technol. **61**(8): 3510-3518. doi: 10.1109/TVT.2012.2207414.

Ma, C.G., Zuo, S.G., He, L., Meng, S., and Sun, Q. 2015. Analytical Model of permanent Magnet synchronous Motor considering slot and high order harmonics. J. Vib., Meas. Diagn. **35**(2): 231-237. doi: 10.16450/j.cnki.issn.1004-6801.2015.02.005.

Nashed, M., and Fayed, A. 2018. Current-Mode Hysteretic Buck Converter With Spur-Free Control for Variable Switching Noise Mitigation. IEEE Trans. Power Electron. **33**(1): 650-664. doi: 10.1109/TPEL.2017.2661984.

Miyama, Y., Ishizuka, M., Kometani, H., and Akatsu, K. 2018. Vibration Reduction by Applying Carrier Phase-Shift PWM on Dual Three-Phase Winding Permanent Magnet Synchronous Motor. IEEE Trans. Ind. Appl. **54**(6): 5998-6004. doi: 10.1109/tia.2018.2862392.

Niu, R, K., Zhu, H. 2020. Design of a centrifugal linear vibrating feeder driven by an eccentric motor. Trans. Can. Soc. Mech.Eng. **44**(1): 49-55. doi: 10.1139/tcsme-2018-0244.

Paramasivan, M., Paulraj, M.M., and Balasubramanian, S. 2017. Assorted carrier-variable frequency-random PWM scheme for voltage source inverter. IET Power Electron. **10**(14): 1993-2001. doi: 10.1049/iet-pel.2016.0580.

Pichan, M., and Rastegar, H. 2017. Sliding-Mode Control of Four-Leg Inverter With Fixed Switching Frequency for Uninterruptible Power Supply Applications. IEEE Trans. Ind.Electron. **64**(8): 6805-6814. doi: 10.1109/TIE.2017.2686346.

Samad, T.B., Pezhman, J., and Nicola, B. 2017. Analytical Modeling of No-Load Eccentric Slotted Surface-Mounted PM Machines Cogging Torque and Radial Force. IEEE Trans. Magn. **53**(12): 1-1. doi: 10.1109/TMAG.2017.2748501

Song, Q., Wan, H.T., Mi, Y.X., and Ye, S.D. 2017. Optimum control strategy of drive torque for pure electric vehicles during acceleration. J. Jiangsu Univ. (Nat. Sci. Ed.). **38**(1): 1-6. doi: 10.3969/j.issn.1671-7775.2017.01.001.

Song, Z.X., Yu, Y.J., Chai, F., and Tang, Y. 2018. Radial Force and Vibration Calculation for Modular Permanent Magnet Synchronous Machine With Symmetrical and Asymmetrical Open-Circuit Faults. IEEE Trans. Magn. **54**(11): 1-5. doi: 10.1109/TMAG.2018.2848724.

Sung, S.J., Jang, G.H., and Lee, H.J. 2012. Torque Ripple and Unbalanced Magnetic Force of a BLDC Motor due to the Connecting Wire Between Slot Windings. IEEE Trans. Magn. **48**(11): 3319-3322. doi: 10.1109/TMAG.2012.2198879.

Sun, X.D., Chen, L., Jiang, H.B., Yang, Z.B., Chen, J.F., and Zhang, W.Y. 2016. High-performance control for a bearingless permanent magnet synchronous motor using neural network inverse scheme plus internal model controllers. IEEE Trans. Ind. Electron. **63**(6): 3479-3488. doi: 10.1109/TIE.2016.2530040.

Tang, X.L., Hu, X.S., Yang, W., and Yu, H.S. 2018. Novel Torsional Vibration Modeling and Assessment of a Power-Split Hybrid Electric Vehicle Equipped with a Dual Mass Flywheel. IEEE Trans. Veh. Technol**. 67**: 1990-2000. doi: 10.1109/TVT.2017.2769084.

Valente, G., Papini, L., Formentini, A., Gerada, C., and Zanchetta, P. 2018. Radial Force Control of Multisector Permanent-Magnet Machines for Vibration Suppression. IEEE Trans. Ind.Electron. **65**(7): 5395-5405. doi: 10.1109/TIE.2017.2780039.

Wang, G.L., Zhou, H.L., Zhao, N.N., Li, C.R., and Xu, D.G. 2018. Sensorless Control of IPMSM Drives Using a Pseudo-Random Phase-Switching Fixed-Frequency N.a. Injection Scheme. IEEE Trans. Ind.Electron. **65**(10): 7660-7671. doi: 10.1109/TIE.2018.2798590.

Wang, R.C., Ding, R.K., and Chen, L. 2018. Application of hybrid electromagnetic suspension in vibration energy regeneration and active control. J. Vib. Control. **24**(1): 223-233. doi: 10.1177/1077546316637726.

Wen, J.B., Song, C.J., Fu, Y., and Guo, P.P. 2018. Rotor structure optimization of permanent magnet synchronous generator built-in type U. J. Jiangsu Univ. (Nat. Sci. Ed.). **39**(2): 194-198. doi: 10.3969/j.issn.1671-7775.2018.02.012.

Xia, J.K., and Gu, L.T. 2014. Investigation of low-noise PWM scheme in automotive heater motor system. Small spéc. Electr. Mach. **42**(5): 56-59. doi: 10.3969/j.issn.1004-7018.2014.05.015

Xia, J.K., and Zhang, X.Y. 2015. Effect of random modulation strategy on system vibration noise in coal preparation plant. Opencast Min. Technol. **32**(12): 68-71. Doi: 10.13235/j.cnki.ltcm.2015.12.021.

Xia, J.K., Wang, X., and He, H.B. 2013. Optimization Design of the Random Switching Frequency Control. Electr. Eng. **14**(1): 26-28. doi: 10.3969/j.issn.1673-3800.2013.01.007.

Xu, B., Xiang, C.L., Qin, Y.C., Ding, P., and Dong, M.M. 2018. Semi-Active Vibration Control for in-Wheel Switched Reluctance Motor Driven Electric Vehicle With Dynamic Vibration Absorbing Structures, Concept and Validation. IEEE Access. **6**: 60274-60285. doi: 10.1109/ACCESS.2018.2875197.

Yin, C.F., Zhang, J.C., and Wang, S.H., Sun, X.Q., and Xu, X. 2017. Influence of damper indicator diagram area on vehicle ride comfort. J. Jiangsu Univ. (Nat. Sci. Ed.). **38**(6): 645-651. doi: 10.3969/j.issn.1671-7775.2017.06.005.

Ze, Q.J., Liang, D.L., Kou, P., and Liang, D. 2018. Reduction of Torque and Voltage Ripple in a Doubly Salient Permanent Magnet Generator. IEEE Trans. Energy Convers. **33**(2): 702-715. doi: 10.1109/TEC.2017.2766126.

Zhao, W.X., Wu, B.Y., Chen, Q., and Zhu, J.H. 2018. Fault-Tolerant Direct Thrust Force Control for a Dual Inverter Fed Open-End Winding Linear Vernier Permanent-Magnet Motor Using Improved SVPWM. IEEE Trans. Energy Convers. **65**(9): 7458-7467. doi: 10.1109/TIE.2018.2795557.

Zhu, J., Li, S.L., Song, D.D., Han, Q.L., and Li, G.H. 2018. Performance parameter analysis of a low speed AFPMSG with stator coreless. J. Jiangsu Univ. (Nat. Sci. Ed.). **39**(4): 445-452. doi: 10.3969/j.issn.1671-7775.2018.04.013.

Zhu, X.Y., Xiang, Z.X., Zhang, C., Quan, L., Du, Y., and Gu, W.W. 2017. Co-Reduction of Torque Ripple for Outer Rotor Flux-Switching PM Motor Using Systematic Multi-Level Design and Control Schemes. IEEE Trans. Energy Convers. **64**(2): 1102-1112. doi: 10.1109/TIE.2016.2613058.

Zhu, J.G., Yan, S.K., Wang, D.L., and Yu, S.B. 2015. Application on Random Switching Frequency SVPWM. Meas. Control Technol. **34**(2): 66-68. doi: 10.19708/j.ckjs.2015.02.018.

Zhu, Z.Q., Xia, Z.P., Wu, L.J., and Jewell, G.W. 2010. Analytical Modeling and Finite-Element Computation of Radial Vibration Force in Fractional-Slot Permanent-Magnet Brushless Machines. IEEE Trans. Ind. Appl. **46**(5): 1908-1918. doi: 10.1109/TIA.2010.2058078.

Zhu, Z.Q., Liu, Y., and Howe, D. 2006. Minimizing the Influence of Cogging Torque on Vibration of PM Brushless Machines by Direct Torque Control. IEEE Trans. Magn. **42**(10): 3512-3514. doi: 10.1109/TMAG.2006.879439.

Zuo, S.G., Gao, L.H., Meng, S., Ma, C.G., and Tn, Q.W. 2015. Double closed-loop nonlinear modeling and analysis for permanent magnet synchronous motor considering rotor magnetic field harmonics. J. Cent. South Univ. (Sci. Technol.). **46**(9): 3217-3223. doi: 10.11817/j.issn.1672-7207.2015.09.008.

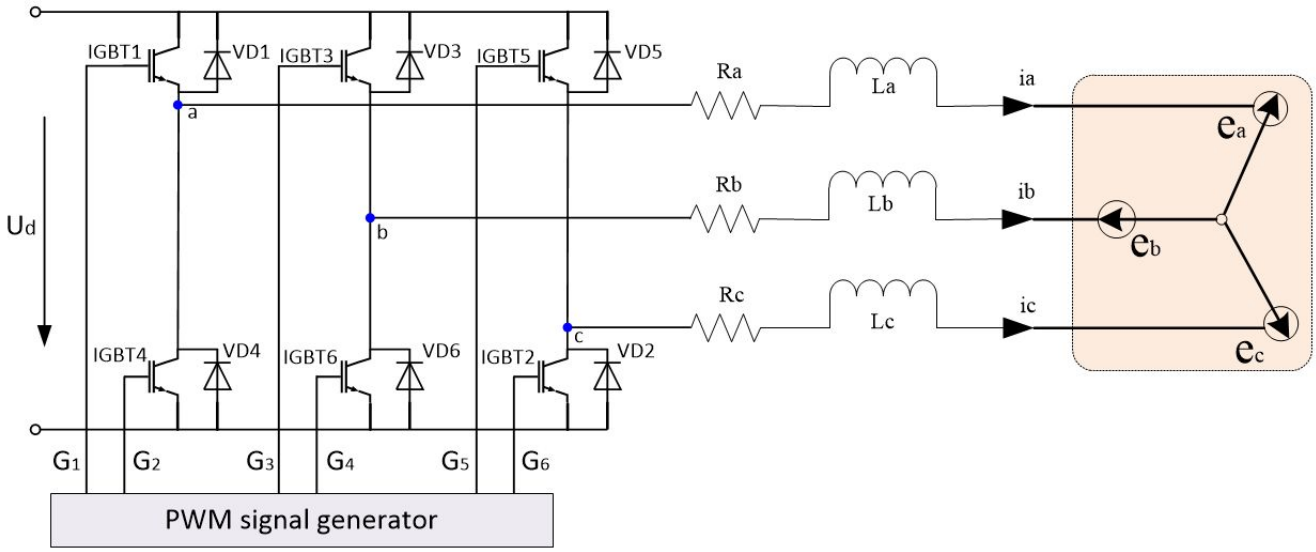

Fig. 1. The drive scheme of inverter-fed PMIWM

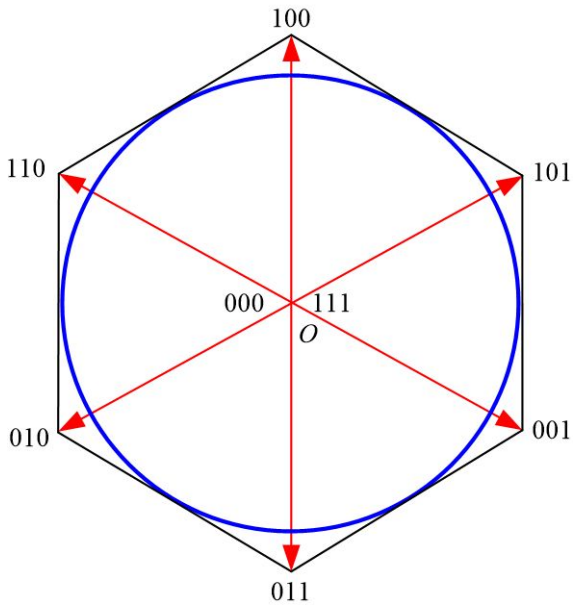

Fig. 2. The voltage space vector diagram of the inverter

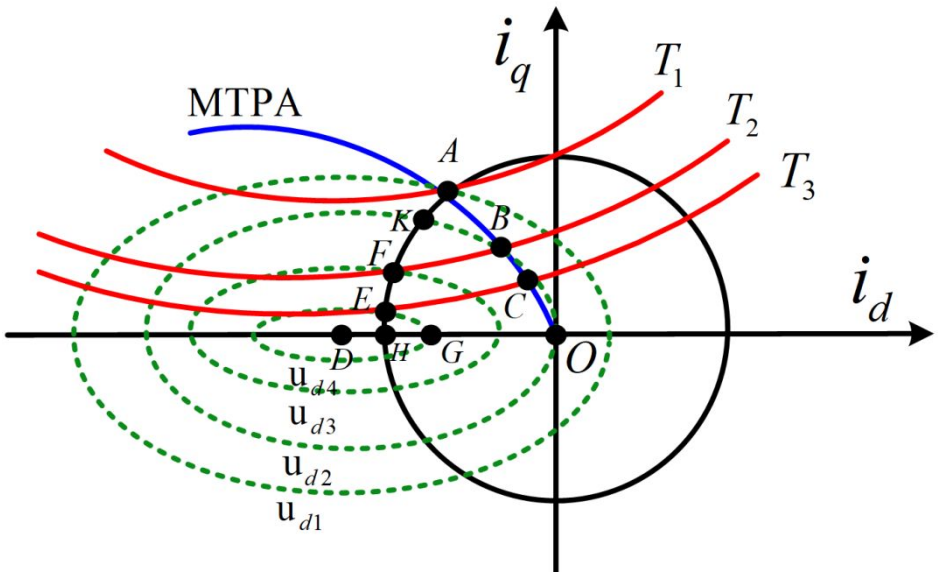

Fig.3 The current trajectory when DC bus changes

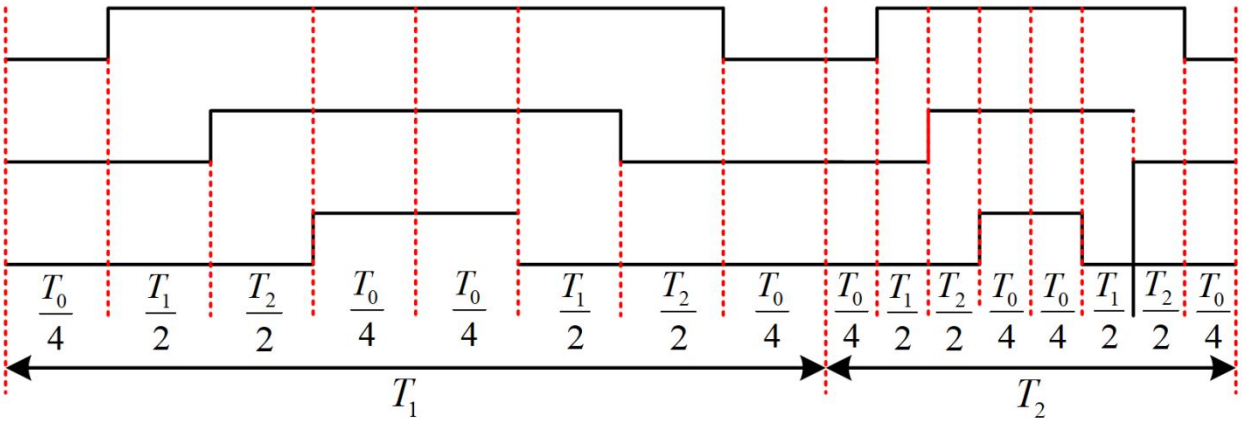

Fig. 4 RSFPWM control diagram

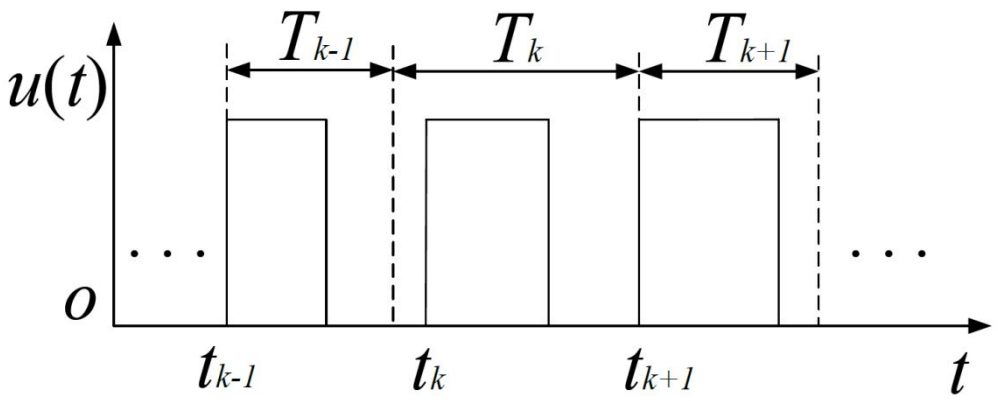

Fig. 5. The diagram of the random switching function

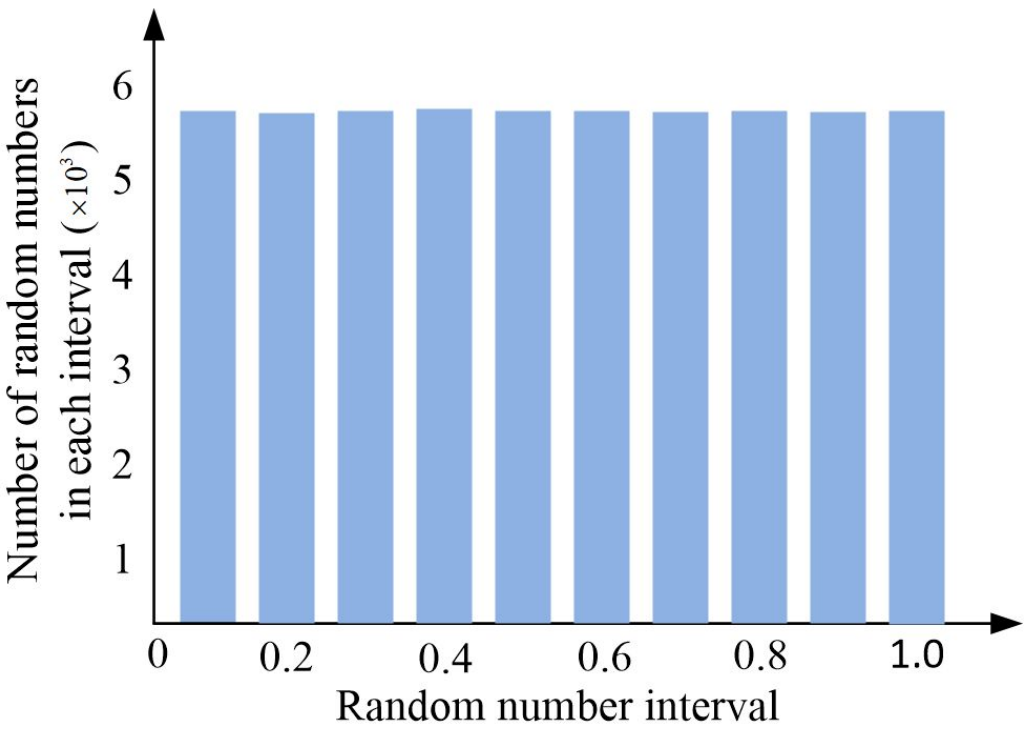

Fig. 6 Random number distribution by mixed congruence method

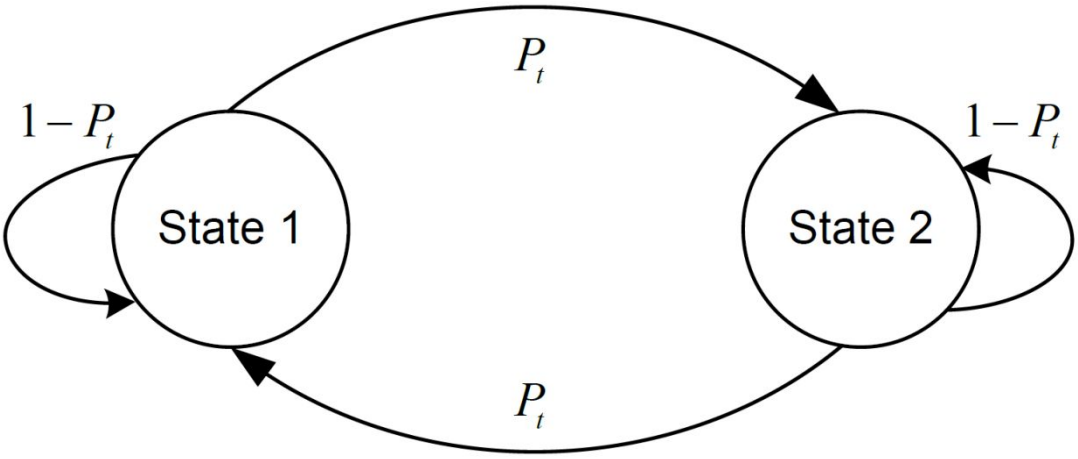

Fig. 7. Two state Markov chain diagram

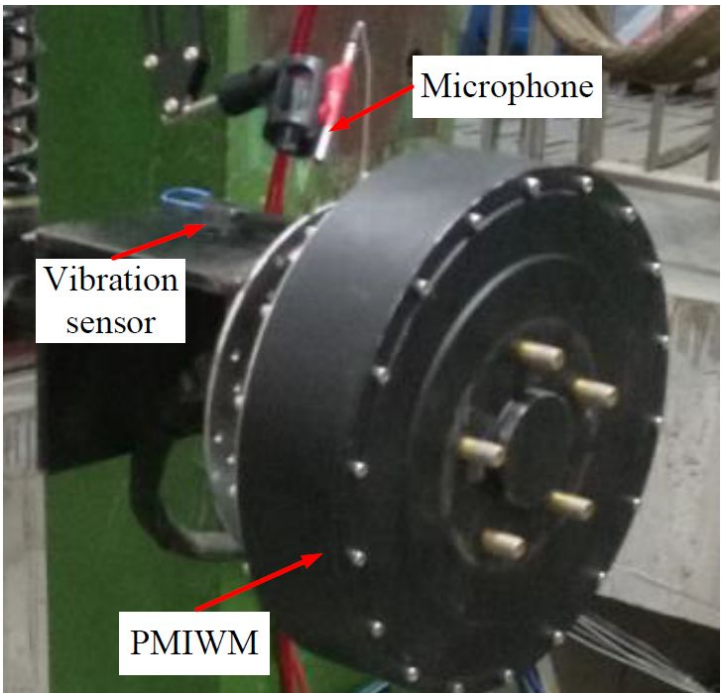

Fig. 8. PMIWM testing platform

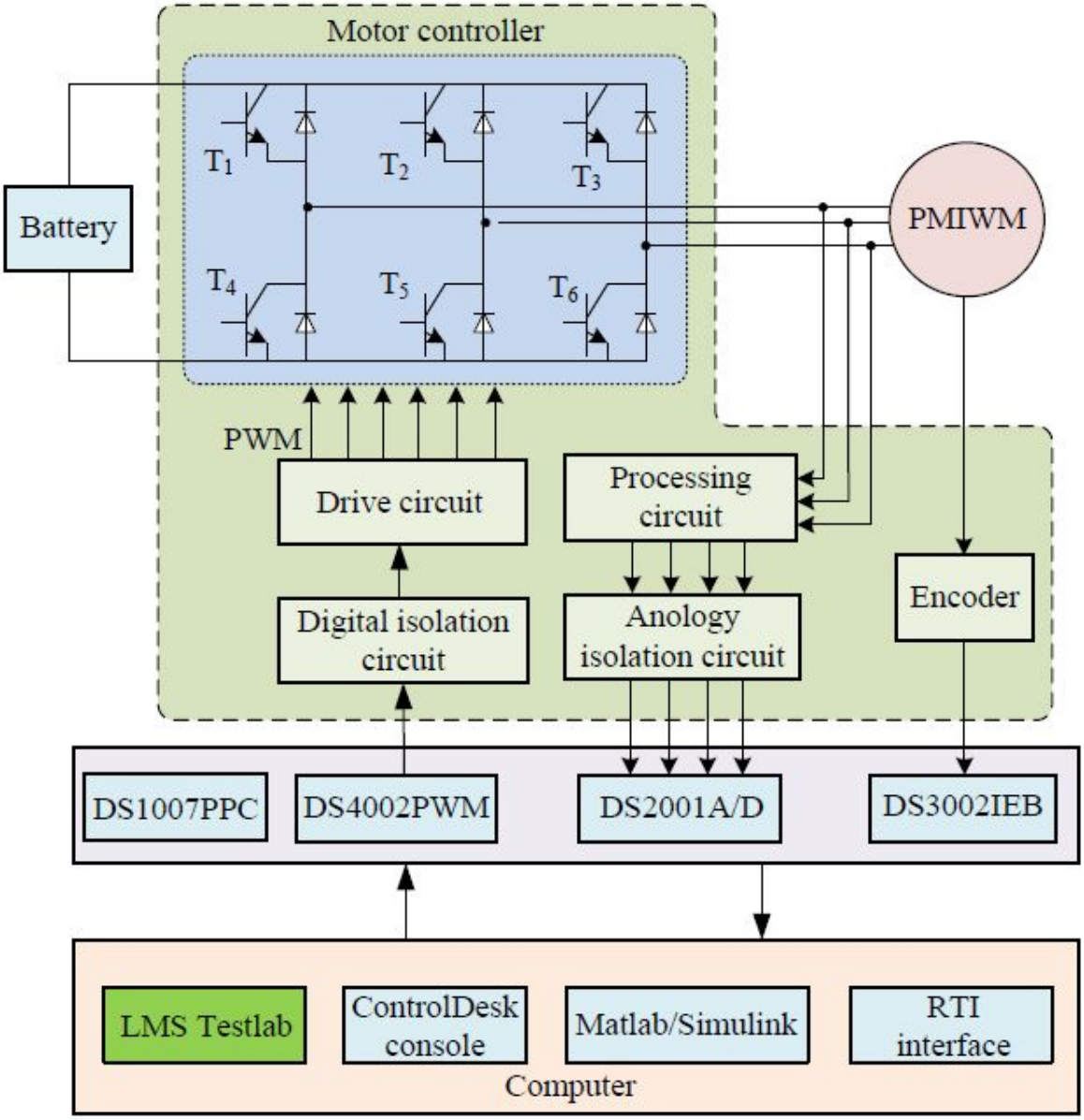

Fig. 9. The diagram of the P0MIWM control system

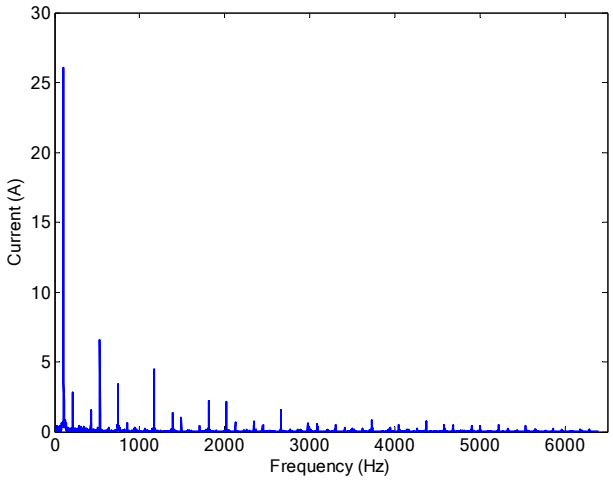

(a)

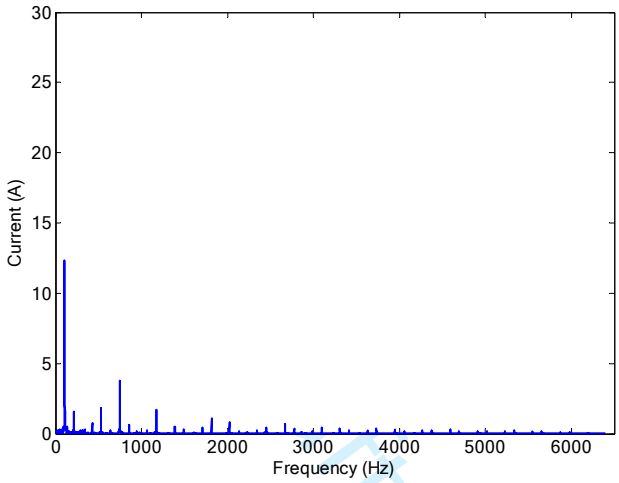

(b)

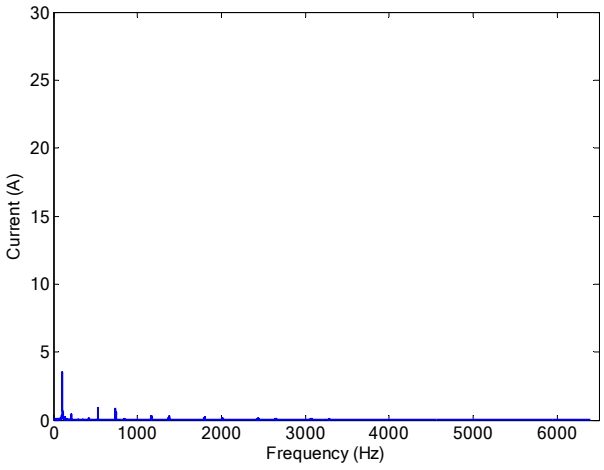

(c)

Fig. 10. Frequency response of phase-a current response under different control methods. (a) Fixed PWM control. (b). RPPPWM control. (c). Proposed RSFPWM control.

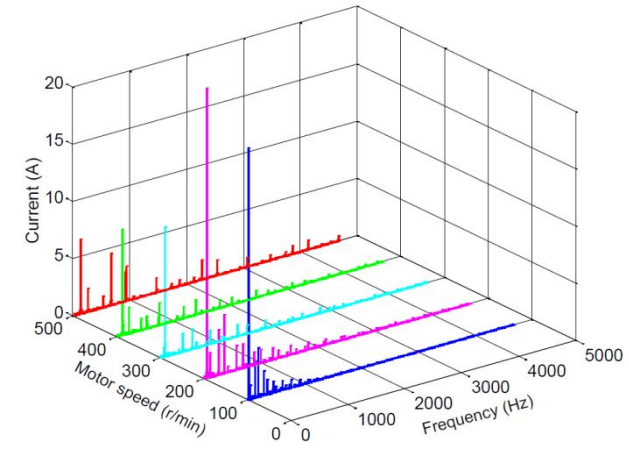

(a)

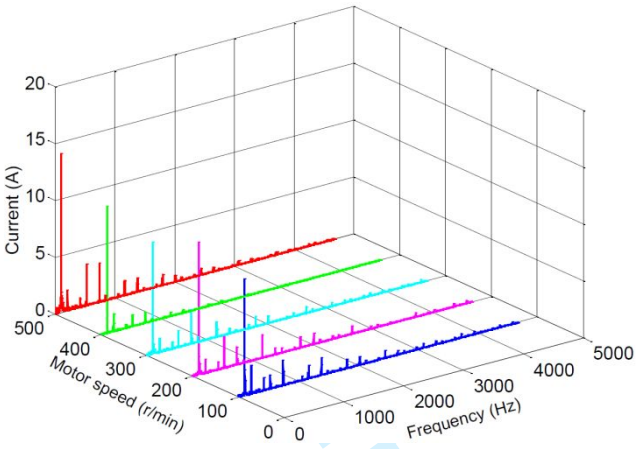

(b)

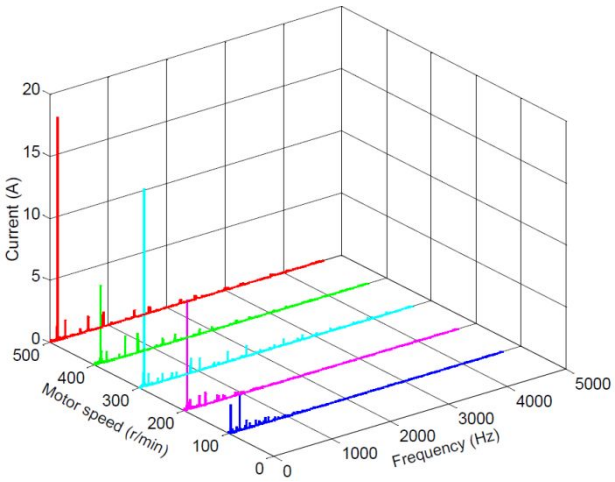

(c)

Fig. 11. The frequency response of phase-a current. (a) Fixed PWM control. (b) RPPPWM control. (c) Proposed RSFPWM control.

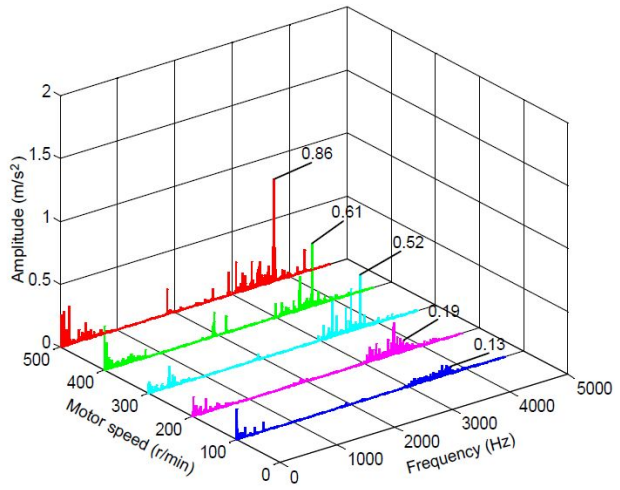

(a)

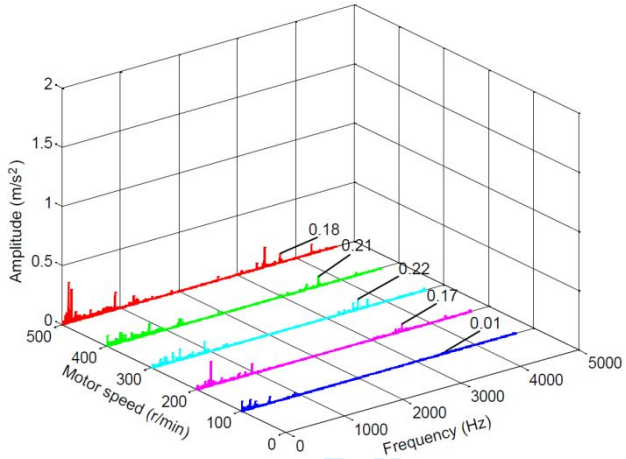

(b)

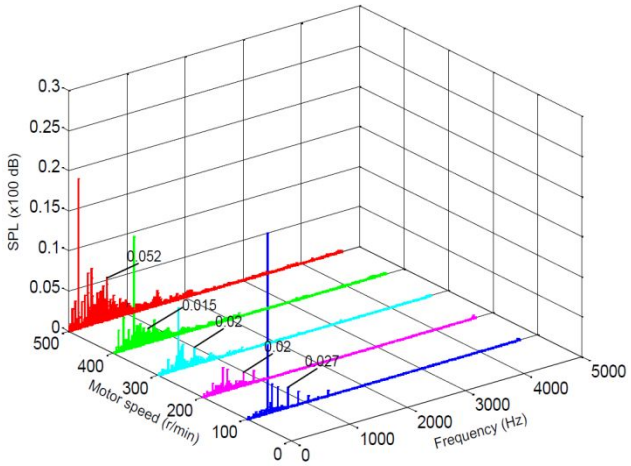

(c)

Fig. 11. The frequency response of PMIWM with fixed PWM control. (a) vibration on the x-axis. (b) vibration on the y-axis. (c) SPL.

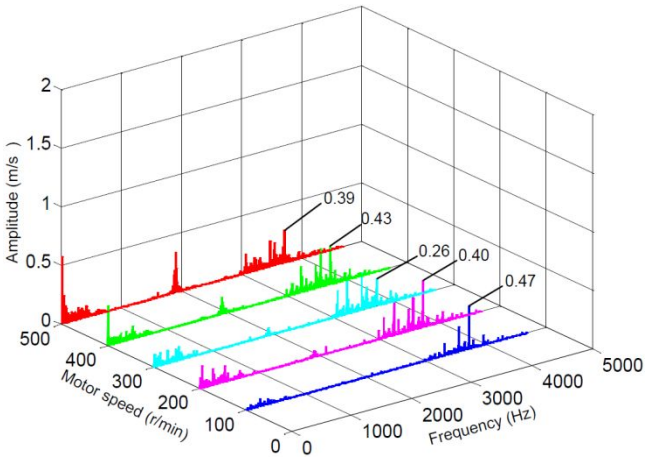

(a)

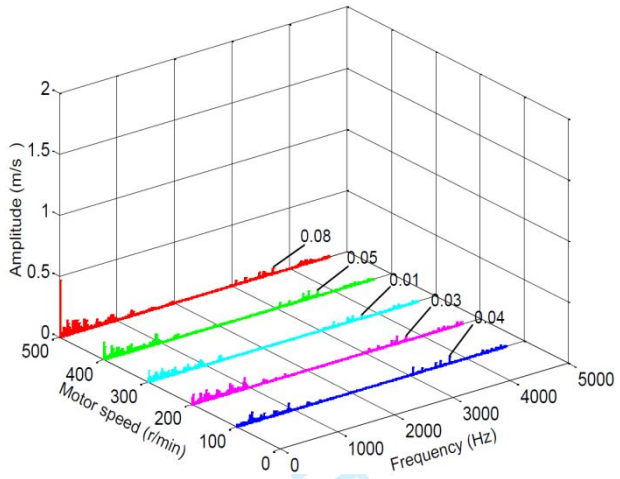

(b)

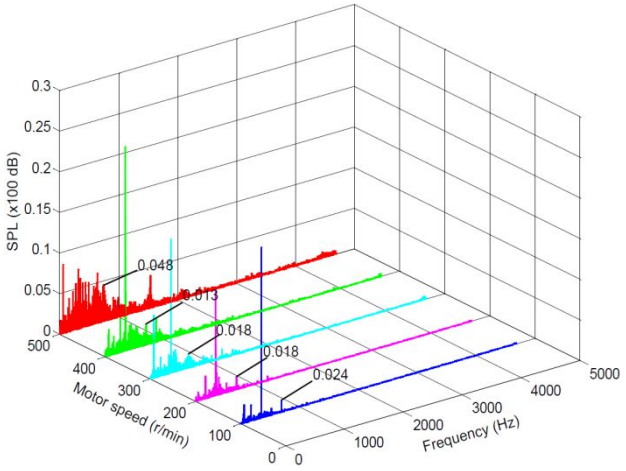

(c)

Fig. 12. The frequency response of PMIWM with the RPPPWM control. (a) vibration on the *x*-axis. (b) vibration on the *y*-axis. (c) SPL.

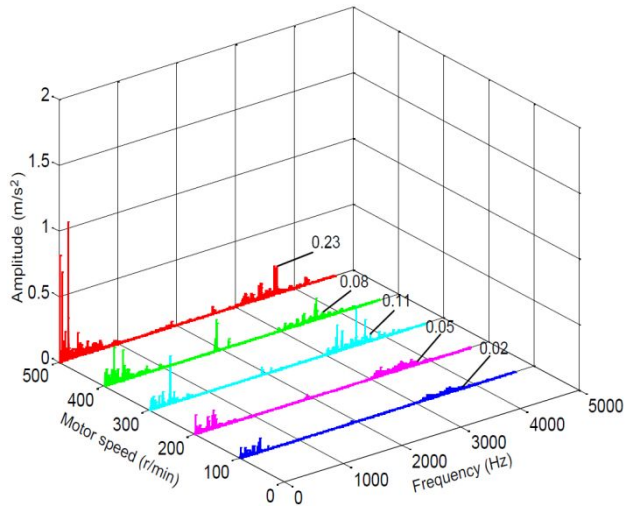

(a)

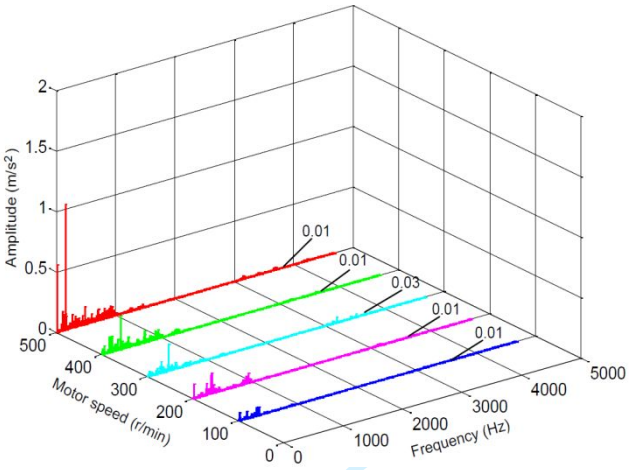

(b)

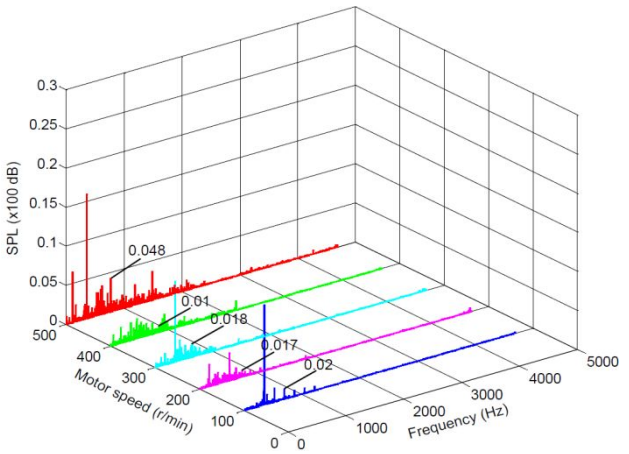

(c)

Fig. 13. The frequency response of PMIWM with the proposed RSFPWM control. (a) vibration on the *x*-axis. (b) vibration on the *y*-axis. (c) SPL.

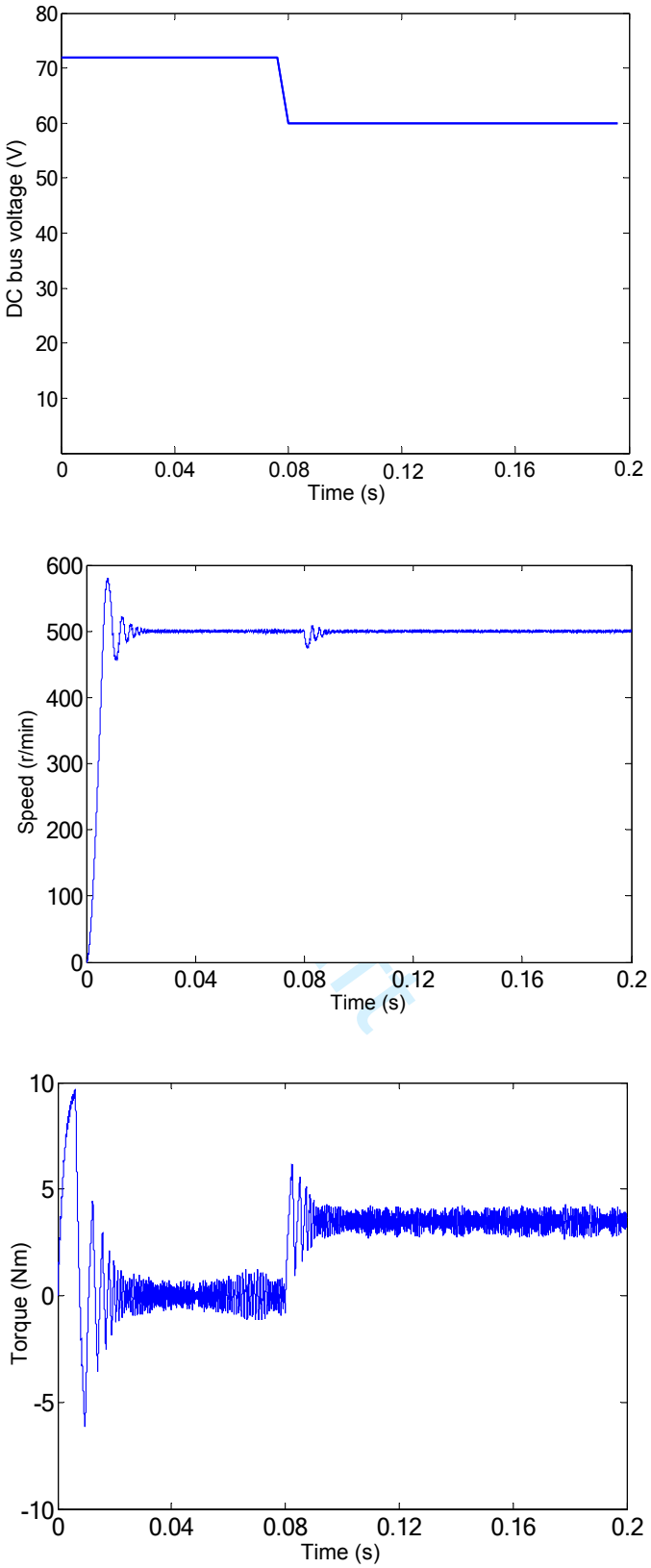

Fig. 14. The response of PMIWM with the proposed RSFPWM control under DC bus voltage fall. (a) DC bus voltage curve. (b) motor speed. (c) Motor torque.

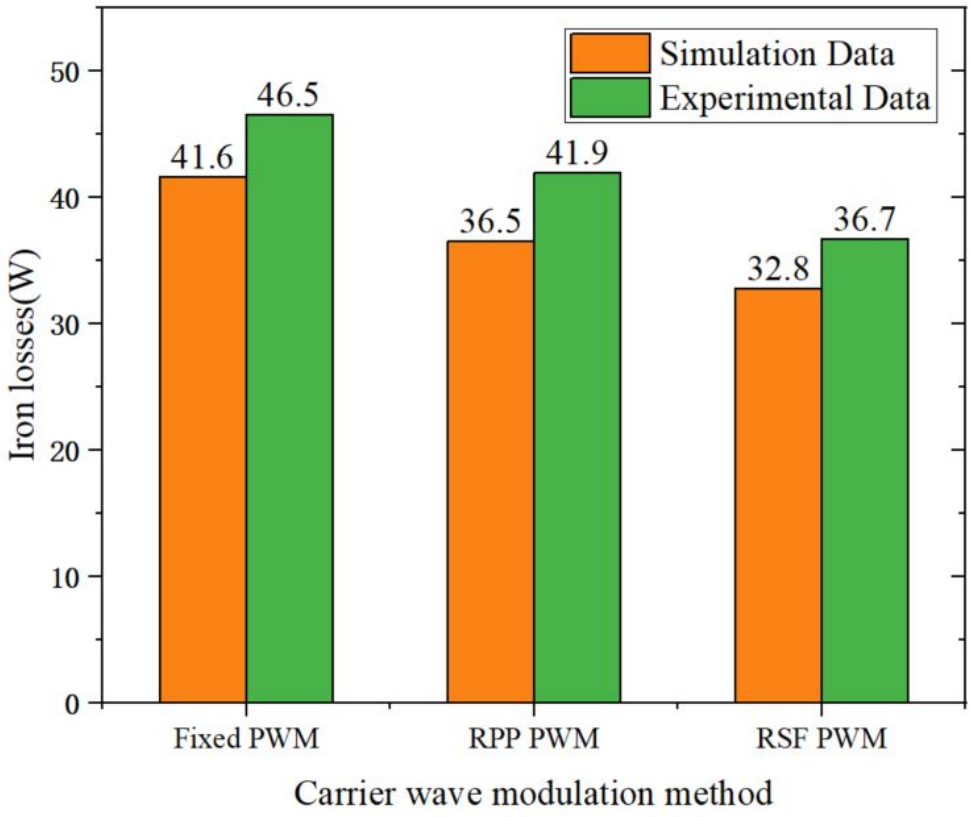

Fig. 15. Inverter losses under different carrier wave modulation methods

TABLE 1.

Simulation results of iron loss

Carrier wave modulation method	Fixed PWM	RPP PWM	RSF PWM
Iron loss (W)	41.6	36.5	32.8

TABLE 2.

PARAMETERS OF THE PMIWM

Parameters	Value	Unit
Nominal power	8	*kw*
Nominal speed	1600	*r/min*
Slot number of stator	36	*N/A*
Pole pair number	16	*N/A*
The outer diameter of the rotor	303	*mm*
The inner diameter of the rotor	283	*mm*
The outer diameter of the stator	273	*mm*
Magnet length	50	*mm*
Magnet width	24	*mm*
Magnet depth	4	*mm*
Slot width	11	*mm*
Phases of the stator winding	3	*N/A*
Wires number per slot	195	*N/A*
Motor length	107	*mm*
Air gap length	0.6	*mm*

TABLE 3.

VIBRATION ACCELERATION UNDER DIFFERENT CONTROL METHODS

Frequency (Hz)	Motor speed (r/min)	Control Schemes		
		Fixed PWM control	RSPPWM control	RSFPWM control
3800 (*x*-axis)	100	0.13	0.47	0.02
	200	0.19	0.40	0.05
	300	0.52	0.28	0.11
	400	0.61	0.43	0.08
	500	0.86	0.39	0.23
3800 (*y*-axis)	100	0.01	0.04	0.008
	200	0.17	0.03	0.01
	300	0.22	0.01	0.03
	400	0.21	0.05	0.01
	500	0.18	0.08	0.01

TABLE 4.

NOISE SPL UNDER DIFFERENT CONTROL METHODS

Frequency (Hz)	Motor speed (r/min)	Control Schemes		
		Fixed PWM control	RSPPWM control	RSFPWM control
800	100	0.027	0.024	0.02
	200	0.02	0.018	0.017
	300	0.02	0.018	0.018
	400	0.015	0.013	0.01
	500	0.052	0.048	0.048

TABLE 5.

EXPERIMENTAL RESULTS OF IRON LOSS

Carrier wave modulation method	Fixed PWM	RPP PWM	RSF PWM
Iron loss (W)	46.5	41.9	36.7